Pergamon

Int. J. Heat Mass Transfer. Vol. 38, No. 9, pp. 1597–1604, 1995

0017-9310/95 $9.50 + 0.00

0017-9310(94)00291-6

Air filtration with moisture and frosting phase changes in fiberglass insulation—II. Model validation

D. R. MITCHELL, Y.-X. TAO† and R. W. BESANT

Department of Mechanical Engineering, University of Saskatchewan, Saskatoon, Saskatchewan, Canada S7N 0W0

(*Received* 7 *February* 1994 *and in final form* 18 *August* 1994)

Abstract—A numerical simulation, employing a local-volume-averaging formulation, was validated for each flow direction (exfiltration/infiltration), based on the experimental temperature and moisture accumulation results obtained in Part I of this study. The predicted results compare well with the measured temperature profiles throughout the insulation slab for both air exfiltration and infiltration. The comparison for the moisture accumulation profiles is generally reasonable, except for locations near the boundaries. Discussion is presented for the model evaluation. The simulation results indicated that air exfiltration and air infiltration through fiberglass insulation can increase the combined heat flux at the cold surface by factors of more than 13 and 6, respectively, compared to dry, no-flow conditions

1. INTRODUCTION

Porous insulation material found within building wall and ceiling structures may experience heat conduction, heat convection due to air motion, radiative heat flux among internal surfaces, moisture diffusion due to water vapor concentration gradients, water vapor convection due to air motion and phase transformation. Moisture transport within the insulation generally takes place either through the process of vapor diffusion, or as a result of the flow of moist air through the insulation. The flow of moist air through such building envelopes is a consequence of pressure differences across the permeable envelope materials caused by wind pressure effects, different temperature gradients inside and outside, or the air circulation fans used within buildings.

If the relative humidity of moist air within the insulation reaches 100%, phase changes in water can occur. In a dynamic process, insulation can become wetter or drier, depending on the combined effects of heat transfer, flow and phase change [2]. Even if the local relative humidity in the porous insulation is below saturation, evidence shows that adsorption or desorption could occur under temperature variation [3]. This sorption process is often accompanied by thermal energy exchange that can alter the local temperatures significantly [3, 4]. Due to the complexity of the interaction among these physical effects, it is often difficult to analyze the data obtained from field measurements [5]. Numerical simulation is often used to investigate the significance of individual physical effects on the thermal performance of a fibrous insulation that undergoes a dynamic process [6, 7]. For coupled heat and moisture transport in fibrous insulation under air exfiltration or infiltration conditions, no comprehensive numerical analysis has been performed for cold climate applications. While numerical analyses prove to be effective, the experimental evaluation of numerical models is limited in the literature.

Motivated by the above observation, we developed a numerical model that corresponds to the similar physical model and boundary conditions established in the experiment (Part I of this study [1]). The model performance is evaluated using the experimental results. The analysis is further carried out to investigate the heat and moisture transfer consequences as related to defective vapor retarders in building envelopes or cracks between building components in cold climates [8, 9].

2. NUMERICAL MODEL

A schematic drawing detailing the geometry for the numerical model is provided in Fig. 1. The phenomena occurring within the insulation are assumed to be one-dimensional, i.e. the vertical side walls are treated as adiabatic and impermeable and the air flow is only in the z direction. Since the experimental work has been conducted to minimize or eliminate any two-dimensional free convection effects occurring within the insulation slab, a one-dimensional numerical model is taken to be sufficient.

The local volume averaging technique [10] is applied to the basic equations of conservation of mass, momentum and energy transfer in order to establish

† Author to whom correspondence should be addressed. Current address: Department of Mechanical Engineering, Tennessee State University, Nashville, TN 37209, U.S.A.

NOMENCLATURE

A	cross-sectional area of the insulation slab [m^2]
c_p	heat capacity at constant pressure [J kg^{-1} K^{-1}]
d	thickness of air gap between cold plate and insulation slab [m]
D_{eff}	effective vapor diffusivity [m^2 s^{-1}]
D	molecular diffusivity [m^2 s^{-1}]
g	gravity [m s^{-2}]
h	grid spacing for numerical model [m]
h_∞	convective heat transfer coefficient [W m^{-2} K^{-1}]
h_m	mass transfer coefficient [m s^{-1}]
Δi	enthalpy of phase change [J kg^{-1}]
k	thermal conductivity [W m^{-1} K^{-1}]
L	total thickness of the insulation slab [m]
$\dot{m}$	rate of mass flow through the insulation [kg s^{-1}]
$\dot{n}$	rate of phase change [kg m^{-3} s^{-1}]
p	pressure [Pa]
q''	heat flux [W m^{-2}]
R	gas constant [J kg^{-1} K^{-1}]
s	saturation
t	time [s]
T	temperature [K]
ΔT	temperature difference [K]
u	velocity [m s^{-1}]
W	water content per unit dry mass [kg moisture/kg of dry solid]
z	coordinate axis [m].

Greek symbols

α	relaxation factor
ε	porosity of insulation material
ρ	density [kg m^{-3}]
τ	tortuosity
ϕ	relative humidity.

Subscripts

a	air
cg	condensable
cond	conduction
conv	convection
eff	effective properties
g	gas phase (air and vapor)
ng	noncondensable
rg	relative to the gas phase
s	solid phase
v	vapor phase
β	liquid or ice phase
∞	ambient conditions
0	reference value.

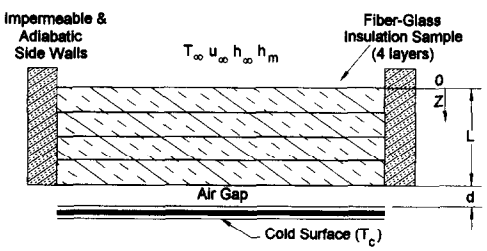

Fig. 1. Geometry used in the numerical modeling.

governing equations which describe the processes occurring within the insulation on a macroscopic level. Using this method, the local properties in the equations are averaged over a representative elementary volume, i.e. the smallest volume that represents the local average properties. For many practical porous media problems, the solution of the volume averaged transport equations is considered adequate [11]. Furthermore, the assumption of local thermal equilibrium is a common simplification procedure to tackle problems involving heat and mass transport in porous material [7]. Detailed information pertaining to the theory involved in the local volume averaging technique can be found in refs. [10, 11].

For the numerical simulations, the liquid capillary velocity is assumed to be zero. According to Vafai and Tien [7], the liquid contained within a porous insulation is essentially immobile, due to a lack of interpore connections, if the level of saturation is below 0.10 (i.e. the water condensate tends to exist in a discontinuous pendular state). For the work presented here, the saturation never exceeds this level; therefore, this assumption is considered valid. Furthermore, since the glass fibers within the insulation have a low volume fraction and the flow velocity through the insulation is low (0.5–1.5 mm s^{-1}), thermal dispersion and mass dispersion are neglected. It is also assumed that, in the frosted or ice crystal region, the frost does not significantly change the homogeneity of the porous matrix. Finally, the analysis is restricted to a rigid porous matrix with constant properties for each constituent and no chemical reactions taking place except those related to hygroscopicity.

The numerical model is intended to model transient one-dimensional processes of simultaneous heat and mass transfer within a porous media (insulation material) subject to pressure driven gas flow and phase changes (i.e. condensation/evaporation, sublimation/ablimation†, and adsorption/desorption). The

† Ablimation means a substance changing from its vapor phase to a solid phase [17]; here, it means frost accumulation from water vapor.

model is based, in part, on one presented by Tao *et al.* [12, 13]. However, this study includes airflow through the porous insulation, which is not considered in refs. [12, 13].

Heat transfer taking place within the fiberglass porous media occurs mainly through conduction and gaseous phase convection. Some radiation effects may have occurred within the insulation, especially in the gap regions near the bottom or top surfaces of the slab (since the insulation is very porous). However, these effects are neglected in this study because they are expected to be less than 10% with respect to conduction and convection [14]. Furthermore, an attempt was made to reduce any radiation effects near the top surface of the sample by coating the inner surface of the test apparatus with aluminum foil.

The reduced set of governing equations is as follows (all properties have been volume averaged, refer to nomenclature).

Thermal energy equation:

$$\rho c_p \frac{\partial T}{\partial t} + \rho_g c_p u_g \left(\frac{\partial T}{\partial z}\right) + \Delta i \cdot \dot{n} = \frac{\partial}{\partial z}\left(k_{eff} \frac{\partial T}{\partial z}\right) \quad (1)$$

where

$$\rho = (1-\varepsilon)\rho_s + \varepsilon s \rho_\beta + \varepsilon(1-s)\rho_g \quad (2)$$

$$c_p = [(1-\varepsilon)(\rho c_p)_s + \varepsilon s(\rho c_p)_\beta + \varepsilon(1-s)\rho_g c_{p_g}]/\rho \quad (3)$$

and

$$k_{eff} = \varepsilon s k_\beta + \varepsilon(1-s)k_g + k_s(1-\varepsilon). \quad (4)$$

Liquid or solid ice phase continuity equation:

$$\frac{\partial \varepsilon_\beta}{\partial t} + \frac{\dot{n}}{\rho_\beta} = 0. \quad (5)$$

Gas phase momentum equation:

$$u_g = -\frac{K_g}{\mu_g}\left[\varepsilon_g\left(\frac{\partial(p_g - p_0)}{\partial z} - \rho_g g\right)\right] \quad (6)$$

where K_g = permeability of the porous media (fiberglass) due to gas flow (air) = $K_{rg}K$.

Gas phase convection and diffusion equations (continuity for each identifiable species):

(a) non-condensable (dry air),

$$\frac{\partial}{\partial t}(\varepsilon_g \rho_{ng}) + \frac{\partial}{\partial z}(\rho_{ng} u_g) = \frac{\partial}{\partial z}\left[\rho_g D_{eff}^{ng} \frac{\partial}{\partial z}\left(\frac{\rho_{ng}}{\rho_g}\right)\right] \quad (7)$$

(b) condensable (water vapor),

$$\frac{\partial}{\partial t}(\varepsilon_g \rho_{cg}) + \frac{\partial}{\partial z}(\rho_{cg} u_g) = \frac{\partial}{\partial z}\left[\rho_g D_{eff}^{cg} \frac{\partial}{\partial z}\left(\frac{\rho_{cg}}{\rho_g}\right)\right] + \dot{n} \quad (8)$$

where it is assumed that:

$$D_{eff}^{ng} = D_{eff}^{cg} = \varepsilon_g D/\tau. \quad (9)$$

Theoretically, the gas phase diffusion equation exists for both the non-condensable and condensable gas components, but equation (7) gives the trivial result that the non-condensable gas flow mass flux was constant. On the other hand, the condensable gas component varied from point to point, so equation (8) was used [equation (7) was not included in the numerical model]. The following equations were used for the accompanying thermodynamic relations:

$$p_{cg} = \rho_{cg} R_{cg} T \quad (10)$$

$$p_{ng} = \rho_{ng} R_{ng} T \quad (11)$$

$$\rho_g = \rho_{cg} + \rho_{ng} \quad (12)$$

$$p_g = p_{cg} + p_{ng}. \quad (13)$$

The Clapeyron equation, for saturation conditions, was taken to be:

$$p_{cg} = p_{cg}^0 \exp\left[-\left[\frac{\Delta i}{R_{cg}}\left(\frac{1}{T} - \frac{1}{T_0}\right)\right]\right]. \quad (14)$$

Adsorption was included in the model for air exfiltration by using the heat of adsorption for Δi in equation (1) and the mass of adsorption from the adsorption isotherm presented by Tao *et al.* [3]. Since air exfiltration dealt with the flow of moist air through an initially dry sample, the need to consider desorption in the exfiltration numerical model did not occur. Furthermore, the insulation material remained 'saturated' during the infiltration process based on the infiltration experimental results and the calculation of W [the mass of vapor adsorbed (adsorbate) per mass of dry sample (adsorbent) $\Delta m/m$]. During air infiltration, this value never fell within the adsorption/desorption isotherm limits. Therefore, neither adsorption nor desorption processes needed to be considered in the infiltration numerical model. The theory related to the modeling of adsorption in the exfiltration numerical simulations is provided in detail in ref. [13].

2.1. *Initial and boundary conditions*

The initial conditions used in the modeling of air exfiltration through the insulation sample remained the same for all of the exfiltration simulations. The entire insulation sample was modeled to be initially at a uniform temperature, with the absorbed liquid volume fraction near zero, a uniform gas density throughout the sample, and with the rate of condensation and the condensable gas density set at zero.

For air infiltration, the initial conditions for the temperature, gas velocity, gas density (condensable and non-condensable), and the rate of moisture accumulation throughout the insulation slab were obtained from the predicted results for the final time step in the exfiltration simulations. Since the exfiltration numerical model predicted moisture accumulation values which were slightly different than those obtained experimentally, the initial condition for the liquid volume fraction profile for air infiltration was not taken from the end of the exfiltration simulations. Instead, although the general shape of the liquid volume fraction profile was implemented from the

simulation results, the values used were modified so that the moisture accumulation in each layer of insulation matched the experimental data (at the end of the exfiltration experiments).

Considering air exfiltration, the boundary conditions for the top surface of the insulation slab were obtained based on the known inlet air conditions ($T_\infty, \phi_\infty, \rho_\infty, h_\infty, h_m$) and the implementation of heat and mass flux balances at this location. The heat flux balance equation at the top surface allowed us to define the temperature on top of the insulation slab using the equation;

$$T(z=0,t) = T_\infty + \frac{k_{eff}}{h_\infty}\frac{\partial T(z=0,t)}{\partial z}. \quad (15)$$

In a similar manner, the mass flow balance allowed us to obtain the condensable gas density on top of the fiberglass slab:

$$\rho_{cg}(z=0,t) = \rho_\infty + \frac{D_{effcg}}{h_m}\frac{\partial \rho_{cg}(z=0,t)}{\partial z}. \quad (16)$$

For the bottom surface of the insulation sample, the measured exfiltration experimental temperature was implemented as a numerical boundary condition. A boundary condition for the condensable gas density was established by assuming that, since the bottom surface was adjacent to the cold region, the conditions were such that the vapor at the bottom of the slab was saturated (sub-freezing temperatures). Thus the Clapeyron equation (14) was used to calculate the condensable gas density at this location.

For the air infiltration numerical model, the temperature boundary conditions were developed by examining the air infiltration experimental test results. The temperature at the top and bottom surfaces of the insulation slab were obtained by curve-fitting the experimental data with respect to time. Boundary conditions for the condensable and non-condensable gas density were determined such that the insulation slab was considered to be under saturation conditions based on the amount of moisture accumulated per dry mass. Therefore, the Clapeyron equation (14) was used to calculate the condensable gas density throughout the entire slab.

2.2. *Method of solution*

The solution method was based on the finite difference forms of the governing equations. The coupled, nonlinear, partial differential equations were solved using the time derivative implicit iteration approach, for which a solution was considered converged when the deviation of any variable from the last iteration was within a specified limit. A relaxation factor was implemented to prevent the numerical model from becoming unstable. For this work, a relaxation value of 0.15 seemed to provide the best results.

In examining the governing equations, there were a total of six unknowns: temperature (T), liquid volume fraction (ε_β), rate of condensation/adsorption ($\dot{n}$), gas velocity (u_g), condensable gas density (ρ_{cg}), and the non-condensable gas density (ρ_{ng}). Once the equations were written in their finite difference forms, they were rearranged to solve for each of the unknown variables using the matrix inversion (or Gauss–Seidel) method. Numerically, the thickness of the insulation slab, L, was 0.10 m (3.92 in) and was divided into 24 equal sections with a grid spacing of 0.00417 m, resulting in a total of 25 nodes for the numerical simulation. Simulations were carried out with a smaller grid spacing: however, this had no effect on the final simulation results. Although experimentally there existed an air gap of spacing d between the bottom surface of the insulation sample and the cold surface (which was used to create the required uniform airflow experimental boundary conditions), the numerical model only dealt with the insulation slab from $z/L = 0$ to $z/L = 1$.

3. VALIDATION OF THE NUMERICAL MODEL

3.1. *Air exfiltration*

Validation of the numerical models for both air exfiltration and air infiltration was obtained by comparing the numerically predicted temperature and moisture profiles to those obtained experimentally. The experimental temperature measurements were obtained for five positions across the insulation sample ($z/L = 0.00, 0.25, 0.50, 0.75, 1.00$). Since the moisture accumulation distribution was only experimentally obtained at the end of each test (i.e. 1, 2 or 3 h tests), continuous moisture accumulation vs time profile comparisons were not possible. Comparisons between the numerical and experimental moisture accumulation profiles for each layer within the insulation sample are performed based on the results obtained at the end of each test period.

Figures 2 and 3 are comparisons of the simulated and measured data for temperature and moisture accumulation for one typical case, the 75% inlet air relative humidity (ϕ), and 1.0 mm s^{-1} air speed (u_g). The air exfiltration numerical model temperature results are well within the experimental uncertainty of ± 0.2 K for temperature and ± 1.0 K in set point temperatures at the two boundaries. The exfiltration of warm air causes warmer temperatures throughout

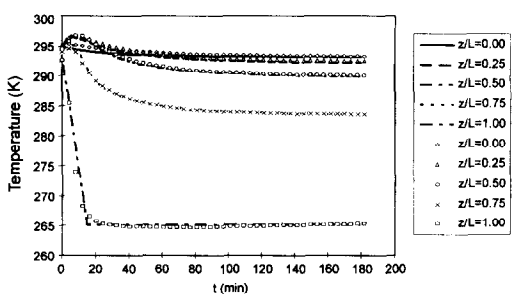

Fig. 2. Air exfiltration temperature profile: $\phi\ (z=0) = 75\%$, $u_g = 1.0$ mm s^{-1}.

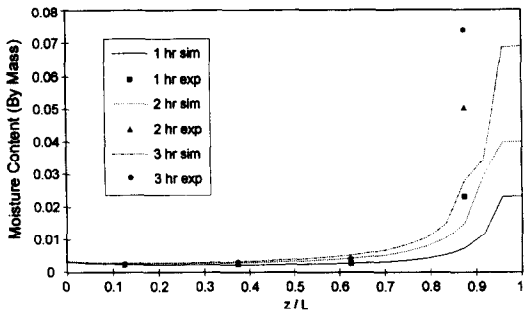

Fig. 3. Moisture profile: air flow rate—10 l min^{-1}, air RH—75%.

most of the insulation, except near the bottom surface where a very large temperature gradient exists. The maximum temperature discrepancy for all of the air exfiltration experiments was less than 1.0 K for a temperature step decrease of 30 K at $z = L$.

Each experimental data point in Fig. 3 represents a ratio of the mass of the accumulated moisture within each insulation layer divided by the dry mass of each layer of insulation. Figure 3 indicates that the majority of the moisture accumulation occurred within the insulation layer closest to the cold surface. With the temperatures within the bottom layer dropping below the saturation temperature, based on the vapor density at such locations, condensation or ablimation takes place. Although moisture adsorption is evident by the temperature rise within the upper regions of the slab immediately after the start of the experiment, the amount of moisture accumulation was much less than within the condensation region (since adsorption deals with the deposition of moisture onto the fiber surfaces in molecular layers).

For these test conditions, the numerical model underpredicts the moisture accumulation within the bottom layer of insulation (the condensation and frosting region). This is partially explained in considering that the numerical model only dealt with the insulation slab itself ($z/L = 0.00$ to $z/L = 1.00$). It does not take into account any moisture/frost which might have accumulated on the bottom surface of the slab (towards the cold plate). Although the temperature comparisons agreed at the five specified locations as shown in Fig. 2, we would not know if the predicted temperature profile within the bottom layer of the insulation slab differed from experimental data at other points without additional temperature sensors.

Radiative heat flux between the cold plate surface and the bottom surface of the insulation slab could have contributed to the additional moisture and frost accumulation measured experimentally. Calculations were carried out, but are not presented here, to estimate the expected radiation flux within the air gap and the effect that this radiation might have on the frost accumulation within this gap. Radiative heat flux is expected to be a primary mode of heat transfer in the gap and this heat flux is expected to be mostly balanced by frost growth on both the cold plate surface and the bottom surface of the insulation slab.

This trend of having the maximum amount of moisture accumulation near the cold surface is similar to the test results obtained with no exfiltration airflow (i.e. vapor diffusion only [15]). In the study by Tao *et al.* [4], it was also found that, during the initial period, more moisture accumulated near the warm side of the insulation slab, while later more moisture and/or frost was found near the cold side of the slab. It should be noted that for operating temperatures above the freezing point, moisture accumulation is not significant even with air infiltration/exfiltration, e.g. Vafai and Tien [7] reported, from their numerical results, a liquid volume fraction of the order of 10^{-4} with the operating temperatures above freezing point. With frosting, however, the air exfiltration effect caused about 45 times as much moisture accumulation; that is the moisture content reached 0.09 by mass or about 4.5×10^{-3} liquid volume fraction for the $\phi = 90\%$ RH and $u_g = 1.0$ mm s^{-1} case.

3.1.1. *Heat flux results—exfiltration.* Calculations were made to determine the heat flux leaving the bottom of the insulation slab based on the experimental results. However, due to radiative heat flux within the air gap between the cold plate and the insulation slab and frost growth on the upper and lower surfaces of the gap, the uncertainty in the heat flux at $z/L = 1.0$ computed from the measured data was nearly 100%. Therefore, the heat flux values were obtained instead based on the numerical simulation results. The conductive heat flux (q''_{cond}) leaving the bottom surface of the insulation slab ($z/L = 1.0$) was determined using the following equation:

$$q''_{cond}(L) = -k_{eff}\left.\frac{\partial T}{\partial x}\right|_{Z=L}. \tag{17}$$

The effective thermal conductivity (k_{eff}) was determined using equation (4). This equation required values for the porosity of the insulation (ε), the degree of saturation at $z = L$ (which is a function of the liquid or frost volume fraction, $s = \varepsilon_\beta/\varepsilon$), and the thermal conductivity of the three individual phases: liquid or frost, gas, and solid (fiberglass) (k_β, k_g, k_s). The temperature gradient at the bottom surface of the insulation was calculated using the backward differencing approximation.

The numerical results were also used to obtain the heat flux results in relation to the convection process over the entire insulation slab. Equation (18) was used to evaluate the sensible convective heat rate per unit flow area (q''_{conv}) for the air not involved in the phase transfer process:

$$q''_{conv} = \frac{\dot{m}c_p\Delta T}{A} \tag{18}$$

where ΔT is the temperature difference between the

Table 1. Numerical heat flux results (2 h data)—air exfiltration

Flow rate [l min^{-1}]	RH [%]	$q''_{cond}(L)$ [W m^{-2}]	q''_{conv} [W m^{-2}]	q''_{total} [W m^{-2}]	$q''_{dry\text{-}noflow}$ [W m^{-2}]	$q''_{total}/q''_{dry\text{-}noflow}$
5	75	32.8	20.8	53.6	10.4	5.2
10	60	40.0	33.4	73.4	9.17	8.0
	75	44.0	35.7	79.7	9.03	8.8
	90	49.4	35.2	84.6	8.95	9.5
15	60	49.1	49.7	98.8	8.43	11.7
	75	55.6	47.7	103.3	8.11	12.7
	90	60.4	46.0	106.4	7.85	13.6

top of the insulation slab and the bottom $[T(z=0)-T(z=L)]$.

For air exfiltration through the envelope of a building, the magnitude of the convective heat flux term represents the amount of energy which would be required to heat the outside or ambient air required to compensate for the amount of air lost through the wall structure during air exfiltration. A heat flux calculation was also performed for a dry insulation sample with no air exfiltration or vapor diffusion (based on the same boundary conditions). This value was calculated using equation (17), with the effective thermal conductivity based on a dry insulation slab, and the temperature gradient taken across the entire insulation slab. A summary of these results is presented in Table 1.

For air exfiltration it is evident that increasing the airflow rate or the inlet air relative humidity results in an increase in the conductive heat flux through the bottom surface of the insulation slab. It is also apparent that increasing the airflow rate had a more significant effect on the total heat flux than increasing the inlet air RH. For example, increasing the inlet air RH from 60 to 90% resulted in a 23.0% increase in the total heat flux for a flow rate of 10 l min^{-1} (u_g = 1.0 mm s^{-1}), and a 23.5% increase in the total heat flux for a flow rate of 15 l min^{-1} (u_g = 1.5 mm s^{-1}), whereas increasing the airflow rate from 5 to 15 l min^{-1} (u_g = 0.5–1.5 mm s^{-1}) for an inlet air RH of 75% resulted in a 70% increase in the total heat flux. The results also indicate that, in comparison to the convection heat flux values, the conductive heat flux through the bottom of the insulation was of similar magnitude. Furthermore, Table 1 shows that the total heat loss due to air exfiltration through the insulation was more than 13 times that for a sample of insulation under similar boundary conditions, which had no moisture accumulation and experienced neither vapor diffusion nor airflow.

It should be noted that, for these simulations, the modeling parameters were kept constant (i.e. the properties of all phases involved, the grid spacing, and all of the empirical constants). However, as discussed above, there is uncertainty in these heat flux results and it is possible that perhaps some of these values might not have been completely accurate for the system under study. Nonetheless, the trends indicated in Table 1 were believed to be quite relevant.

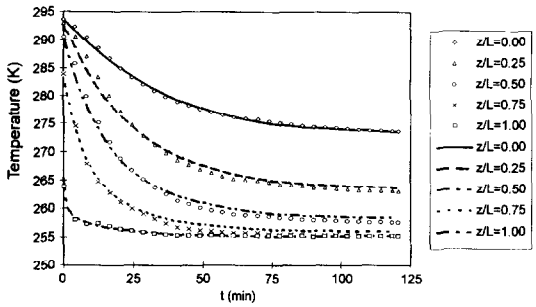

Fig. 4. Temperature profile: air flow rate—10 l min^{-1}, exfiltration air RH—75%.

3.2. *Air infiltration*

The graphs shown in Figs. 4 and 5 compare the experimental and numerical temperature and moisture accumulation results for air infiltration with the flow velocity at u_g = 1.0 mm s^{-1} (10 l min^{-1}) and the exfiltration inlet air RH at 75%. Comparisons for all of the test conditions studied in Table 2 indicated a maximum temperature discrepancy between the experimental and numerical results of less than 3 K for a temperature difference of 33 K across the slab of insulation.

Figure 5 indicates that, in the upper layer of the insulation slab (z/L = 0 to z/L = 0.25), the moisture accumulation was over-predicted. In the remaining layers of insulation the predicted moisture accumu-

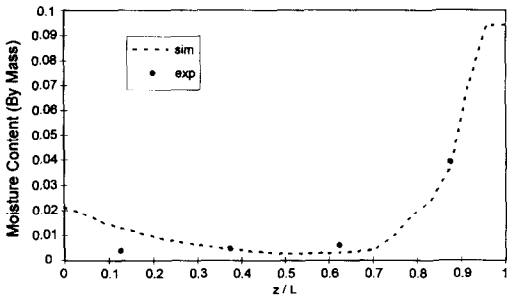

Fig. 5. Moisture profile: air flow rate—10 l min^{-1}, exfiltration air RH—75%.

Table 2. Numerical heat flux results—air infiltration

Test conditions (exf = exfiltration)	q''_{cond} [W m^{-2}]	q''_{conv} [W m^{-2}]	q''_{total} [W m^{-2}]	$q''_{dry\text{-}noflow}$ [W m^{-2}]	$q''_{total}/q''_{dry\text{-}noflow}$
5 l min^{-1}, 75% exf RH	4.51	15.2	19.7	7.39	2.67
10 l min^{-1}, 60% exf RH	0.766	25.2	26.0	6.06	4.29
10 l min^{-1}, 75% exf RH	0.691	24.6	25.3	5.90	4.29
10 l min^{-1}, 90% exf RH	0.743	24.5	25.2	5.86	4.3
15 l min^{-1}, 75% exf RH	0.017	28.9	28.9	4.54	6.36

lation values agreed well with those obtained experimentally. The discrepancy between the data and the simulation in the top layers of insulation could be reduced and possibly eliminated by varying the diffusion coefficient across the insulation slab, decreasing the diffusion for small values of z. During the development of this model, it was discovered that, for air infiltration, the diffusion coefficient (D) had a significant influence on the resulting temperature and moisture accumulation profiles. Although a value of 0.26×10^{-4} m^2 s^{-1} (based on a binary diffusivity between air and water vapor) performed quite well for the air exfiltration simulations, it did not work well for air infiltration, where sublimation occurred in the bottom layer and ablimation or condensation occurred in the upper layers. Instead, a constant value of 0.52×10^{-4} m^2 s^{-1} was used for all of the air infiltration simulations. However, examination of the measured and simulated results suggests that perhaps the diffusion coefficient should not remain constant across the insulation slab. It may also suggest that the assumption of local thermal equilibrium may not be satisfied for air infiltration, where the flow direction was the same as the temperature gradient. Furthermore, a local thermal instability in the flow could exist due to the heat release during condensation or ablimation, which is similar to a fluid being heated from below (Benard problem [16]). A flow instability could have occurred if, due to the energy released during the re-deposition of moisture in the upper layers of insulation, the local temperature gradient became reversed relative to the temperature gradient across the entire slab of insulation. These refinements are beyond the scope of this paper and, therefore, they need further research.

3.2.1. *Heat flux results—infiltration.* The calculation for the conductive heat flux through the bottom surface of the insulation sample, based on the numerically predicted air infiltration results, was carried out using the same equations as for air exfiltration [equations (4) and (17)]. This also applied to the convective heat flux component, which was calculated using equation (18). For air infiltration this represents the amount of sensible heating which would be required to heat the cold air entering the building envelope due to air infiltration to a temperature of 20°C. The results obtained for the five test conditions for air infiltration are presented in Table 2.

Table 2 indicates that heat conduction through the bottom surface was small compared to convective heat transfer, except for low air speeds. Furthermore, relative to a dry insulation sample which experiences neither vapor diffusion nor forced airflow, infiltration increased the total heat loss by more than a factor of 6. This ratio is independent of the temperature to which the air is heated during the infiltration process, but is strongly dependent on the air infiltration rate.

4. SUMMARY AND CONCLUSIONS

This work was aimed at modeling the processes taking place within wall or roof fiberglass insulation with frosting effects and showing the influence of airflow through the insulation (exfiltration/infiltration) on the heat loss to the exterior of a building. The development and validation of this numerical model to simulate such processes will aid in studying various other test conditions. Some discrepancies do currently exist between the numerical predictions and the experimental results, near the cold surface gap for frost accumulation related to air exfiltration and near the warm surface for moisture removal and deposition during air infiltration. Possible explanations for these differences have been made; however, more experimental and numerical research work will be required to resolve the discrepancies entirely. Based on the results presented, the physical importance of reducing or eliminating any air flow through insulated structures with the use of a properly installed vapor retarder has been made clear.

The results obtained through this work lead to the following conclusions.

Air exfiltration

(1) The air exfiltration numerical model predicted the temperature profile throughout the insulation slab quite well, with a maximum discrepancy of 1 K for a total temperature step change of 30 K for airflow speeds of 0.5–1.5 mm s^{-1} and relative humidities of 60–90%. The model also predicted the moisture accumulation profiles within the upper three layers of the insulation to within ± 0.002 mass content ratio. However, the model under-predicted the amount of moisture accumulation within the bottom layer of insulation (closest to the cold plate) by approx. 50%.

(2) By increasing the exfiltration inlet air RH from

60 to 90%, the numerical model predicted an increase in the conductive heat flux at the bottom cold surface of 23% for both the 1.0 mm s^{-1} and the 1.5 mm s^{-1} air speeds. Increasing the airflow rate has a more substantial influence on the conductive heat flux results (e.g. an increase in the air speed from 0.5 s to 1.5 mm s^{-1}, for the 75% inlet RH case, resulting in a 70% increase in the conductive heat flux at the bottom cold surface).

(3) Under the air exfiltration conditions studied, the implied heat losses due to convection and conduction at the cold surface were similar in magnitude, and combined they exceeded the heat flux of a dry insulation sample with no airflow by more than a factor of 13.

Air infiltration

(1) The air infiltration numerical model predicted the temperature profiles throughout the insulation slab with a maximum discrepancy of 3 K for a temperature difference across the insulation slab of 33 K for airflow speeds of 0.5–1.5 mm s^{-1}. Furthermore, this model predicted the moisture accumulation profiles well, except in the upper region of the insulation slab (top layer of insulation) where it over-predicted the amount of moisture accumulation.

(2) For air infiltration, the conductive heat flux through the bottom surface of the insulation was practically negligible, except at the lowest airflow speed. The results indicate that, under the air infiltration conditions studied, the main mode of heat loss for an insulated building envelope would be through convection and would exceed that for dry insulation with no air motion through the insulation by more than a factor of 6.

REFERENCES

1. D. R. Mitchell, Y.-X. Tao and R. W. Besant, Air filtration with moisture and frosting phase changes in fiberglass insulation—I. Experiment, *Int. J. Heat Mass Transfer* **38,** 1587–1596 (1995).
2. K. Vafai and H. C. Tien, A numerical investigation of phase change effects in porous materials, *Int. J. Heat Mass Transfer* **32,** 1261–1277 (1989).
3. Y.-X. Tao, R. W. Besant and C. J. Simonson, Measurement of the heat of adsorption for a typical fibrous insulation, *ASHRAE Trans.* **98**(2), 495–501 (1993).
4. Y.-X. Tao, R. W. Besant and K. S. Rezkallah, The transient thermal response of a glass-fiber insulation slab with hygroscopicity effects, *Int. J. Heat Mass Transfer* **35,** 1155–1167 (1992).
5. C. P. Hedlin, Effect of moisture on thermal resistances of some insulations in a flat roof system under field-type conditions, ASTM STP 789, pp. 602–625 (1983).
6. M. K. Kumaran, Heat, air and moisture transport through building materials and components: can we calculate and predict?, *Proceedings of the Sixth Conference on Building Science and Technology*, pp. 129–144, University of Waterloo (1992).
7. K. Vafai and H. C. Tien, A synthesis of infiltration effects on an insulation matrix, *Int. J. Heat Mass Transfer* **33,** 1263–1280 (1990).
8. NBC, *National Building Code of Canada.* National Research Council, Canada (1990).
9. ASTM, *Water in Exterior Building Walls: Problems and Solutions* (Edited by T. A. Schwartz). ASTM STP 1107, Philadelphia, PA (1991).
10. M. Kaviany, *Principles of Heat Transfer in Porous Media.* Springer, New York (1991).
11. S. Whitaker, Simultaneous heat, mass and momentum transfer in porous media: a theory of drying. In *Advances in Heat Transfer* (Edited by J. P. Hartnett and T. F. Irvine Jr), Vol. 13. Academic Press, New York (1977).
12. Y.-X. Tao, R. W. Besant and K. S. Rezkallah, Unsteady heat and mass transfer with phase changes in an insulation slab: frosting effects, *Int. J. Heat Mass Transfer* **34,** 1593–1603 (1991).
13. C. J. Simonson, Y.-X. Tao and R. W. Besant, Thermal hysteresis in porous insulation, *Int. J. Heat Mass Transfer* **36,** 4433–4441 (1993).
14. P. Boulet, G. Jeandel and G. Morlot, Model of radiative transfer in fibrous media–matrix method, *Int. J. Heat Mass Transfer* **36,** 4287–4297 (1993).
15. Y.-X. Tao, R. W. Besant and K. S. Rezkallah, Heat and moisture transport through a glass-fiber slab with one side subjected to a freezing temperature. In *Water in Exterior Walls: Problems and Solutions*, ASTM STP 1107, pp. 92–104 (1991).
16. S. Chandrasekhar, *Hydrodynamic and Hydromagnetic Stability*, pp. 9–75. Oxford University Press, Oxford (1961).
17. A. V. Luikov, *Heat and Mass Transfer in Capillary-Porous Bodies* (Translated by P. W. B. Harrison and Translation Edited by W. M. Pun), p. 254. Pergamon Press, Oxford (1966).